www.DeepakPublishing.com

Simms, L., et al. (2013): JoSS, Vol. 2, No. 2, pp. 235-251
(Peer-reviewed Article available at www.jossonline.com)

www.JoSSonline.com

Orbit Refinement with the STARE Telescope

Lance M. Simms, Don Phillion, Wim De Vries, Vincent Riot, Brian J. Bauman and Darrell Carter

Lawrence Livermore National Laboratory, Livermore, CA, 94550, USA

Abstract

The proposed Space-Based Telescopes for Actionable Refinement of Ephemeris (STARE) mission, which will consist of a constellation of nano-satellites in low Earth orbit (LEO), intends to refine orbits of satellites and space debris to less than 100 meters uncertainty in order to help satellite operators prevent collisions in space. To prove this is possible, a prototype STARE payload was used to refine the orbit of NORAD 27006 using a series of six ground-based images captured over a 60 hour period. The refined orbit, based on the first four observations made within the initial 24 hours allowed for prediction of the satellite's trajectory to within less than 50 meters over the following 36 hours, as verified by the final two observations taken within that period. This paper describes the tools and methodology used to capture the images of NORAD 27006 and refine its orbit—the same ones that will be used during the STARE mission. The details of verifying the accuracy of the orbit over the next 36 hours are then presented, lending credence to the capability of STARE to accomplish its mission objectives.

1. Introduction

Accurately predicting the location of a satellite in low Earth orbit (LEO) at any given time is a difficult enterprise. The primary reason for this is the uncertainty in the quantities needed for the equations of motion. Atmospheric drag, for instance, is a function of the shape and mass of the satellite, as well as the density and composition of the tenuous atmosphere through which it is moving. In a typical scenario, all of these quantities are poorly known (Vallado and Finkleman, 2008). And over many days, other difficult-to-model phenomena, such as solar radiation pressure and gravitational field perturbations due to earth solid body and ocean tides, influence the movement of the satellite (Vallado, 2005). These uncertainties and the incompleteness of the equations of motion lead to a quickly growing error in the position and velocity of any satellite being tracked in LEO.

In order to account for these errors, the Space Surveillance Network (SSN) must repeatedly observe the set of nearly 20,000 objects it tracks. With each new observation, it is able to fit the orbit and generate a fresh Two-Line Element (TLE) that contains the orbital information for the object. The problem is that even with these continuously modified TLEs, the positional uncertainty of an object can be as large as approximately

Corresponding Author: Lance Simms - simms8@llnl.gov

Copyright © A. Deepak Publishing. All rights reserved.

1 km (Vetter, 2007). This lack of precision leads to approximately 10,000 false alarms per expected collision. With these large uncertainties and high false alarm rates, satellite operators are rarely motivated to move their assets after a collision warning is issued.

The motivation behind the Space-Based Telescopes for Actionable Refinement of Ephemeris (STARE) mission is to reduce this 1 km uncertainty to 100 m or less for objects in LEO. Since the probability of collision scales with the area of the positional uncertainty, a reduction in linear uncertainty by a factor of ten would reduce the false alarm by a factor of one hundred. Thus, STARE can reduce the current false alarm rate of ~10,000 per expected collision to only ~100. On average, any given satellite will then only receive a small number of warnings during its lifetime. With a false alarm rate this low, satellite operators can consider taking action to reposition their assets when a warning is issued. STARE will accomplish its goal by providing a dedicated platform of nano-satellites in LEO capable of observing any object related to a potential conjunction predicted by the SSN several times over a 24-48 hr window.

The aim of this paper is not to describe the concept of the STARE mission in detail. For a comprehensive overview of STARE, the reader is referred to Simms et al. (2012). Rather, the intention here is to show that orbital predictions with accuracy better than 100 m are possible within the STARE framework. This was demonstrated by using a prototype STARE payload equipped with a visible wavelength telescope, CMOS sensor, and GPS antenna and receiver to capture a set of six observations of NORAD 27006 from the ground. The first four observations were used to refine the orbit of the object. The last two were used to validate the predictive accuracy.

This paper is organized as follows. First, a brief overview of the STARE satellite and constellation is given. This includes details on the STARE telescope and the on-board data processing that is performed to extract the star and streak locations. Next, the methods used to select and observe the target NORAD 27006 over a 60-hr period are described. Following this is a detailed description of the computational methods used to fit the orbit with the first four observations and predict its location in the last two. Finally, the errors limiting the accuracy of the observations and predictions are discussed, along with a prospective outlook for the STARE constellation.

2. Space-Based Telescopes for Actionable Refinement of Ephemeris

2.1. The STARE Constellation

The proposed STARE mission calls for a constellation 18-24 3U CubeSats[a] operating in LEO. The satellites in the fleet will be evenly distributed in three orbital planes in a ~700 km polar orbit, which will ensure that almost any target is observable in a 24-hr period.[b] The CubeSats will operate in a "follow-up" mode, only monitoring targets that are perceived by the more general survey and tracking networks to be under threat. In other words, STARE is not intended to replace the SSN or any other surveying instruments, such as the planned Space Fence (Haines and Phu, 2011). It is only intended to refine the predictions made by the latter so that the information is more "actionable," providing an operator with a more reliable warning so that they can make a more informed decision whether to reposition their satellite.

To do so, each STARE payload must be equipped with an imaging system capable of observing targets as small as 0.1 m diameter, moving at speeds of up to 10 km s^{-1} at distances of up to 1000 km.

2.2. The STARE Payload

As shown in Figure 1, the prototype STARE payload is equipped with a small telescope that feeds a 1280 × 1024 Aptina MT9M001 CMOS detector with 5.2 micron pixels. The telescope has a primary mirror aperture of 85 mm and a focal length of 178.8 mm, making the F-number approximately F/2. The optical

[a] A CubeSat is a nano-satellite standard that consists of base 1U cubes of dimension 10 cm × 10 cm × 10 cm. A 3U CubeSat is three of these cubes stacked together.

[b] Detailed system studies indicates minimal performance degradation if the constellation is not arrayed in three evenly space planes.

Copyright © A. Deepak Publishing. All rights reserved.

system thus provides fairly good sky coverage with a field of view (FOV) of 1.98° × 1.58°.

Below the sensor assembly is a processor board that handles communication between all the various peripherals. These peripherals include SD cards for image storage, a Thermo-Electric Cooler (TEC) that provides the sensor with cooling down to -10°C, and a GPS board essential for precise time stamping of the images.

The GPS antenna rests on a 10 cm × 7 cm aluminum ground plane located on the side of the payload. The ground plane and a thin aluminum box surrounding the processor board have been shown through testing to be essential for maximizing the signal from the GPS satellites and reducing electromagnetic interference from clocks on the main processor board. The first several versions of the payload were unable to obtain a GPS fix without them.

The prototype STARE payload by itself is not capable of controlling or determining the attitude of the satellite, nor can it communicate directly with receivers on the ground. The Boeing Colony II bus[c] into which it is inserted (not shown in Figure 1) is responsible for these tasks. When operating in orbit, a STARE satellite will be sent pointing coordinates and a time corresponding to the pass of a pre-selected target. The Colony II bus will then point the satellite to the designated field. The temporal information will be fed to the payload, which will start capturing a series of ten images at the designated time.

While the Colony II bus was not involved in the ground-observation campaign described in the following sections, the rest of the flight-based observational procedure was followed exactly.

3. Setup and Method for STARE Ground Observations

To mimic the pointing that will be provided by the Colony II bus, the prototype STARE payload was mounted in a representative plastic frame, and this frame was then attached to a motorized Celestron telescope mount capable of tracking sidereal motion,

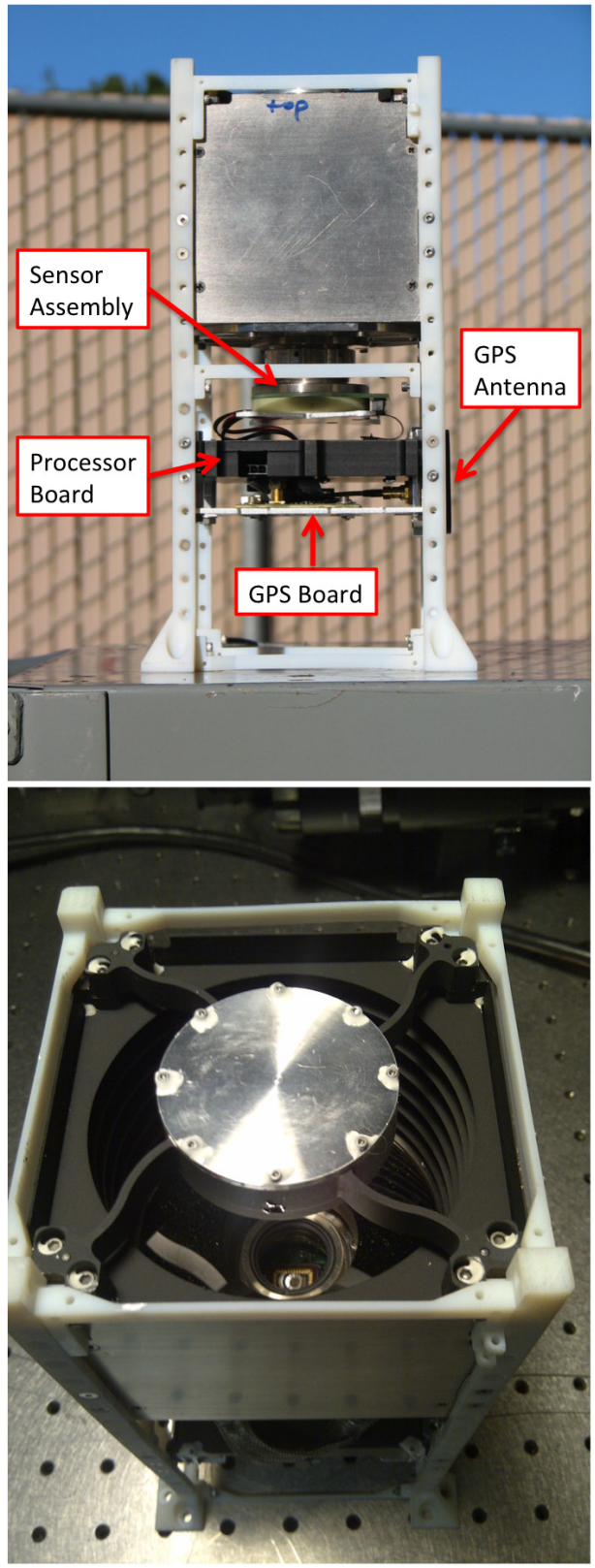

Figure 1. (Top) The prototype STARE payload in its plastic frame with selected components labeled. (Bottom) View looking down into telescope. The primary and secondary mirrors are visible, as well as the CMOS sensor.

[c] The Colony II bus is fabricated by Boeing for the National Reconnaissance Office (NRO) CubeSat Office.

Copyright © A. Deepak Publishing. All rights reserved.

as shown in Figure 2. The mount was placed outside at Lawrence Livermore National Laboratory in a location with minimum ambient lighting and adequate sky coverage. The coordinates of the location are listed in Table 1.

Table 1. GPS coordinates of observing location for the ground-campaign described in this paper.

Latitude (degrees)	Longitude (degrees)	Elevation (m)
37.68960	121.71176	177.6

Finding a target that could be observed 4-5 times over a 48-hr period proved to be difficult for the exact reasons that the STARE constellation is being proposed:

- Targets are only visible ~1.5-2.0 hours before sunrise and after sunset;
- Targets with low elevation are obscured by scattered ambient light; and
- Only targets with very high inclinations will be repeatedly observable from the same location over the 48-hour window.

To find a suitable target, the brightest objects in the NORAD catalog were propagated around the date of January 14, 2013, the expected start date of the ground campaign. Any target that had passes with elevation greater than 30° every 14 hours or less was kept for consideration; all others were rejected. After this filtering, very few candidates remained. NORAD 27006, or SN27006, was finally chosen because it had a set of six high passes over a 60-hour window. Data for these passes is presented Table 2.

The properties of NORAD 27006 make it a good target for this study. It is an SL-16 Rocket Booster (R/B), a spent rocket body of the Soviet Zenit family. It has a length of 32.9 m and a diameter of 3.9 m (http://www.russianspaceweb.com), giving it a sufficiently low average magnitude[d] of ~3.8. It has a perigee of 992 km and an apogee of 1014 km, placing it high enough above the earth to make the effects of atmospheric drag less severe. And with an inclination of 99.1°, it is repeatedly observable over the same spot on Earth.

Figure 2. Photograph of pseudo-STARE prototype payload shown in 1 attached to Celestron telescope mount. Adjacent to the payload is an Orion finder-scope used for fine pointing. The cart next to the mount holds two power supplies to deliver the 3.3, 5.0, and 12.0 Volt lines that the Colony II provides in addition to the computer that serves as the data acquisition system.

For some of the passes listed in Table 2, stray light from sodium street-lamps and obstructions to the south made it so that the maximum elevation of NORAD 27006 did not present the optimum observing opportunity. In these cases, the Heavens Above website (http://www.heavensabove.com/) was used to select a better region of the sky to capture the target (indicated by the Start RA and DEC).

Once the specific pointing of the telescope was decided for each pass, a corresponding STARE observation command packet was generated. The command packet contains the UTC week and UTC second corresponding to the start of the observation, along with other information, such as the number of images to take and the control temperature for the sensor. All data was collected in this manner.

[d] The STARE imager does not include a passband filter, and as such, captures most of the light between 400 and 800 nm. It has a detection limit of about 10th magnitude (in a 1-second exposure).

Copyright © A. Deepak Publishing. All rights reserved.

4. Data Analysis

The entire STARE data pipeline—from capturing the images of the target to predicting its position at the time of the expected conjunction—is shown in Figure 3. Each step in the process is described in the following subsections. Any differences between how the data was processed on the ground for SN27006 and how it will be processed during the developmental stages (i.e. flying prototypes) of the STARE mission are noted.

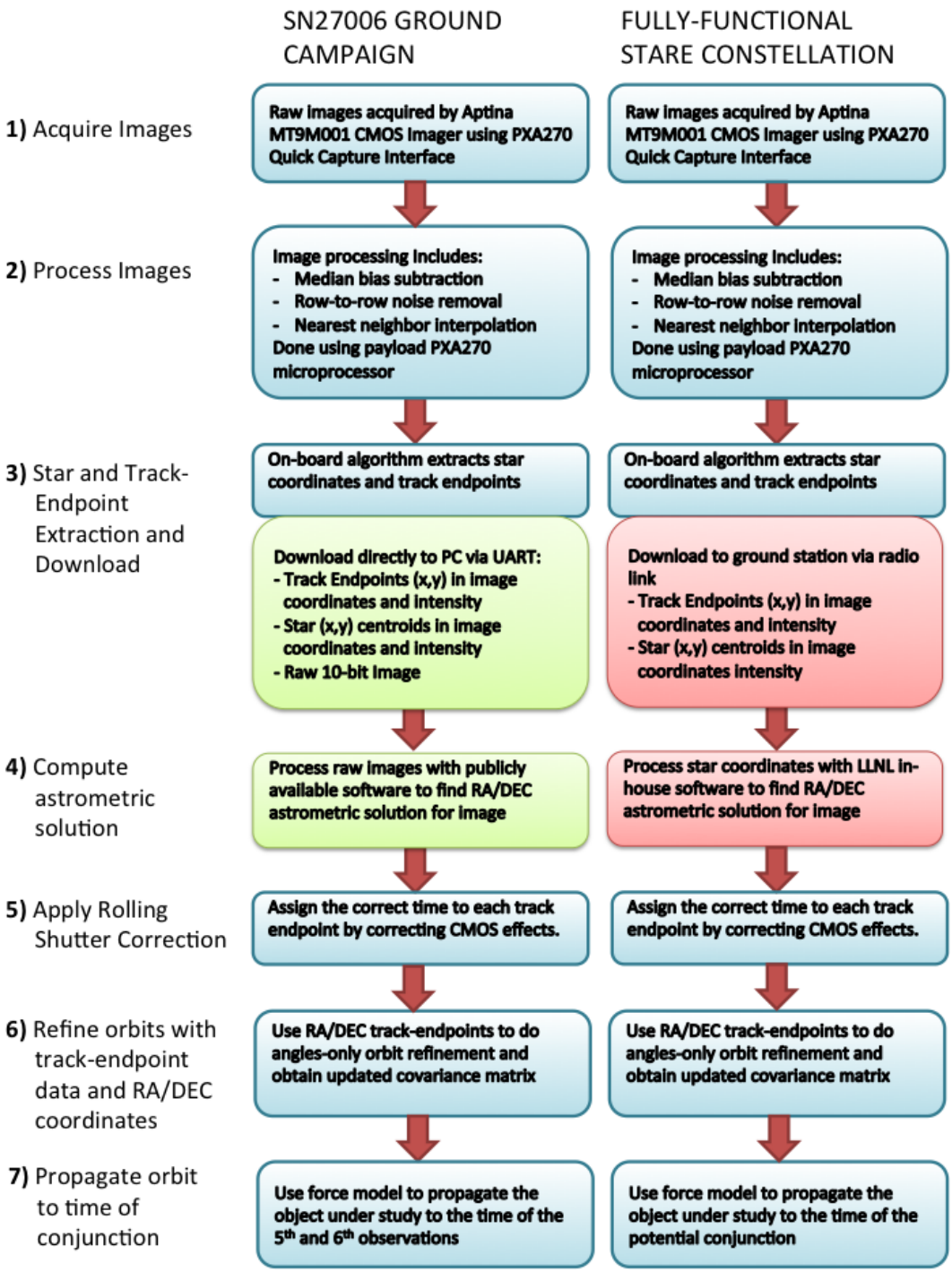

Figure 3. A flow diagram outlining the STARE data pipeline. On the far left are the steps involved in the pipeline, labeled 1-7. For each step, there are two associated boxes. The left box corresponds to the procedure used during the SN27006 ground campaign. The right box corresponds to the one proposed to be used during the STARE mission. The color-coding is meant to illustrate the subtle differences between the two. The blue color indicates that there is no difference. The green means that it was used during the ground campaign in place of the final procedure (red) that would be implemented in the STARE mission. The differences are explained in the text.

Copyright © A. Deepak Publishing. All rights reserved.

Table 2. Selected quantities for the planned observations of NORAD 27006. The date and time of the observation are in UTC. The Start RA (Right Ascension) and Start DEC (Declination) correspond to the equatorial coordinates of the target during the observation time. The range (approximate) is the physical distance between the STARE telescope and the target. The maximum elevation is the approximate highest angle the satellite reached in the sky during its pass.

Date	Time (UTC)	Time Elapsed (hh:mm)	Start RA (degrees)	Start DEC (degrees)	Range (km)	Max. Elevation (degrees)
1/14/13	13:56:07.66	+00:00	154.95	40.89	1204	58.77
1/15/13	02:40:43.61	+12:45	10.09	56.45	1078	71.63
1/15/13	12:43:45.55	+22:48	262.75	52.22	1577	37.42
1/15/13	14:26:09.55	+24:30	151.83	11.71	1646	32.43
1/16/13	03:10:47.62	+37:15	320.30	58.65	1527	40.37
1/17/13	01:58:27.36	+60:02	80.17	42.06	1278	65.77

4.1. Image Acquisition

For each observation, ten images are acquired by the Aptina MT9M001 CMOS sensor and stored in the payload processor memory (RAM). Immediately before taking these images, a series of ten bias frames with 80μs exposure time is collected. A median bias frame is created from these and stored to the SD card on the processor board.

4.2. Image Preprocessing

The raw images from the observation are first corrected by doing bias subtraction using the median bias frame obtained in the previous step. They are then subjected to a moving-windowed median filter that removes row-to-row noise. Finally, a nearest neighbor interpolation scheme is applied to correct for dead and hot pixels. All of these corrections are applied using the PXA270 payload microprocessor.

4.3. Star Centroid and Track Endpoint Extraction and Download

The final, cleaned observation images are then run through an automated on-board algorithm that identifies the star centroid and track endpoint[e] positions (in pixel coordinates) as well as their relative brightnesses. For full details on the algorithm, the reader is referred to Simms et al. (2011).

In short, the algorithm uses a matched filter approach that accounts for the optical system Point Spread Function (PSF) to simulate a series of track-ends. The simulated track-end that has the minimum residual after subtraction from the real track-end yields the best estimate of the endpoint.

When the STARE constellation is fully functional, the amount of data that will be passed down to the ground from the satellites will be restricted to the star centroids and track endpoints, their relative brightnesses, and the corresponding GPS timing information, along with a small amount of other telemetry. However, for the 27006 ground-campaign described in this paper, all ten raw images and the median bias from each observation were downloaded as well. This was for purposes of display and verification of the algorithm performance.

Another important difference worth mentioning is that in the case of this ground campaign, the download was simply a transfer from the payload to a laptop PC over a 115,200 UART link. For the case of the full STARE constellation, the data will first be sent over the 115,200 UART link to the Colony II bus. Then, when the satellite is properly positioned above a ground station, it will be transferred to the station over a 57600 bps radio downlink.

4.4. Computing an Astrometric Solution

After the data from all observations has been down-

[e] Note that the STARE telescope will maintain a fixed pointing during an exposure. Thus, stars will appear as points and the debris or satellite under investigation will appear as a streak in the image.

Copyright © A. Deepak Publishing. All rights reserved.

loaded, the next step is to convert the star and track endpoint positions extracted from each image from pixel coordinates to coordinates on the sky. To accomplish this, the star centroid positions from each image of SN27006 were fed into a World Coordinate System (WCS) solver obtained from nova.astrometry.net. The output of the WCS solver allows one to map the pixel coordinates to Right Ascension (RA) and Declination (DEC).

While the open-source WCS software from nova.astrometry.net was used for this ground campaign, this will not be the case for the STARE prototypes. The prototypes will eventually use a LLNL-developed star tracker routine to obtain a WCS solution for each observation. At the time of writing, however, this code was not yet available for use.

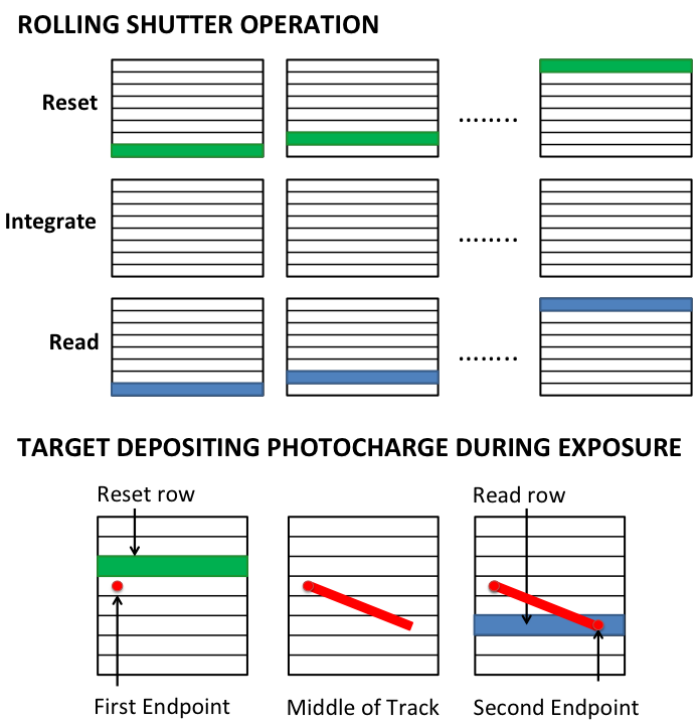

Figure 4. The top portion of this figure shows how the rolling shutter operation of a CMOS detector works. The bottom illustrates its effect on an image of a moving object. At left, the row containing the object has just been reset. This time corresponds to the first streak endpoint. In the middle, all pixels are integrating charge while the object crosses the field. At right, the row containing the object has just been read. This time corresponds to the second streak endpoint.

4.5. Rolling Shutter Correction for Track Endpoints

The GPS reports a single exposure start time for each image. Since the stars are essentially stationary during the exposure (aside from any jitter or smear), this time can easily be associated with the stellar positions reported in the image. However, because the Aptina MT9M001 is a CMOS based detector with a rolling shutter and the target object is moving during the exposure, the reported time does not, in general, coincide with either track endpoint.

For each streak, the times of the streak start and the streak end must be determined using the exposure start time, the exposure duration, and a set of specific rolling shutter equations. This is because the rows are not exposed during the same time intervals, as shown in the top portion of Figure 4. It should be noted that while this figure shows an integration time longer than the time taken to read or reset the frame, an integration time as short as the time taken to read one row is possible.

The bottom left frame of Figure 4 shows the time at which photo-charge from the target is first allowed to accumulate during an exposure. There is a delay between the time this row is reset, t_{EP1}, and the exposure start-time reported by the GPS, t_0. The delay is the product of the row number (Y_{EP1}) and the row time (t_{row}), yielding a streak start endpoint time of:

$$t_{EP1} = t_o + Y_{EP1} \times t_{row} . \qquad (1)$$

For the Aptina MT9M001 and the 17 MHz clock used, the row time is t_{row} = 87.9 microseconds. In the bottom middle frame of Figure 4, rows are integrating while the target streaks across the frame. Again, this will only be the case when the integration time is longer than the frame read or reset time (1024 × t_{row}). The bottom right frame of Figure 4 shows the time at which the row containing the target is finally read out. Now, the delay between resetting and reading the first row is the integration time, $t_{integration}$. And since there is a delay between reading the first row and reading the row of the second endpoint, Y_{EP2}, the time at which the latter

Copyright © A. Deepak Publishing. All rights reserved.

row is actually read out is given by:

$$t_{EP2} = t_o + t_{integration} + Y_{EP2} \times t_{row}. \quad (2)$$

4.6. Angles-Only Batch Least Squares Orbit Refinement

The final product of the first five steps of the STARE data pipeline is a set of N measurements of the location of the target in equatorial coordinates (RAt_i, $DECt_i$) at the UTC times t_i.[f] When STARE is fully functional, N will typically be somewhere between 5-10. Simulations show that for a set of N measurements over a 24-hour period, the size of the uncertainty ellipsoid for a given target decreases with increasing N until N=10 or so, after which it remains relatively constant (Simms et al., 2012).

Before beginning the fitting process, one final step remains. The RA_i and DEC_i values must be corrected for stellar aberration due to the source motion and by correcting for the light speed delay, an action made possible since the orbit is approximately known beforehand.

After all corrections have been applied, the N observations are fit using a force model batch least squares method. This method requires that the observational errors be known and that there be no biases, criteria that are met by the STARE measurements. The full details of the methodology for batch least squares are beyond the scope of this paper. For a good treatise of the subject, the reader is referred to Montenbruck and Gill (2001). Only a short overview will be presented here.

Following the notation of Montenbruck and Gill, the N measurements of the target collected by the STARE telescope form a column vector z.

$$\mathrm{z} = \begin{pmatrix} z_1 \\ \vdots \\ z_n \end{pmatrix}.$$

Specifically, for the angles-only approach implemented here, the components of z are the RA and DEC of the track centers (note that n actually equals $2N$, since there are two angles for each measurement). To properly fit the orbit, the number of measurements must be at least 4, or n must be at least 8.[g]

The state vector of the target, x, is a time-dependent, m-dimensional vector consisting of the position r and velocity v of the satellite:

$$\mathrm{x} = \begin{pmatrix} \mathrm{r}(t) \\ \mathrm{v}(t) \end{pmatrix}.$$

In this case m=6, but in general x may also contain free parameters that affect the force and measurement model. A number of different coordinate systems can be used, but for simplicity, consider an Earth Centered Inertial (ECI) coordinate system. x may be evolved in time using an initial value x_o and an ordinary differential equation of the form dx/dt=f(t,x).

The actual observations in z can be compared to the modeled observations in x(t) using

$$\mathrm{z} = \mathrm{h}(\mathrm{x_o}) + \epsilon,$$

where h denotes the model value of ith observation as a function of the time t_i and the state x_o at the reference epoch t_o. represents the difference between the actual and modeled observations due to measurement errors. The errors are assumed to be randomly distributed with zero mean.

The goal of the least squares orbit determination method is to find a state x_o^{lsq} that minimizes the loss function

$$J(\mathrm{x_o}) = \rho^T \rho = (\mathrm{z} - \mathrm{h}(\mathrm{x_o}))^T (\mathrm{z} - \mathrm{h}(\mathrm{x_o})),$$

where T denotes the transpose. What makes the prob-

[f] The "t" on RAt (Right Ascension) and DECt (Declination) originally stood for topocentric. The observed RAt and DECt for an orbiting object depend upon the observer location. The meaning has been generalized to mean any observer location, orbital as well as ground-based. Of course, the RA and DEC values for the stars depend in an immeasurably small way upon the observer location on or near the earth. One only has to be careful with the aberration attributable to the observer motion. For notational convenience, the "t" will be omitted in subsequent references.

[g] For any fixed atmospheric drag, a force model orbit can always be found which exactly fits three observations. This is because there are six orbital parameters excluding the atmospheric drag and six angles for three observations. With at least four observations, one can determine the atmospheric drag as well.

Copyright © A. Deepak Publishing. All rights reserved.

lem difficult is that h is a highly non-linear function of the unknown vector x_o. One solution is to linearize all quantities around a reference state x_o^{ref}:

$$\rho \approx z - h(x_o^{ref}) - \left(\frac{\partial h}{\partial x_o}\right)(x_o - x_o^{ref}) = \Delta z - H\Delta x_o,$$

where $\Delta xo = (x_o - x_o^{ref})$ is the difference between the state vector that is being optimized and the reference state. **H** is the Jacobian, which gives the partial derivatives of the modeled observations with respect to the state vector at the reference epoch to. It is a $2n \times 6$ matrix, row partitioned into the row vector blocks $\partial RA_1/\partial x_o$, $\partial DEC_1/\partial x_o$, $\partial RA_2/\partial x_o$, $\partial DEC_2/\partial x_o$, ..., $\partial RA_n/\partial x_o$, $\partial DEC_n/\partial x_o$. Because of the non-linearity of the equations of motion, the partial derivatives must all be calculated numerically.

With this linearization, the orbit refinement problem becomes a linear least-squares problem of finding a x_o^{lsq}, such that

$$J(x_o) = \rho^T\rho = (\Delta z - H\Delta x_o)^T(\Delta z - H\Delta x_o)$$

is minimized. The solution to this problem is given by

$$\Delta x_o = (\mathbf{H}^T\mathbf{W}\mathbf{H})^{-1}(\mathbf{H}^T\mathbf{W}\Delta z).$$

W is a weighting matrix that represents the observational errors. If these errors are uncorrelated, then W is diagonal with elements σ_i^{-2}, where σ_i is the rms error in the *i*th observation. For the SN27006 measurements, the errors (which are set by the accuracy of the endpoint finding algorithm, which in turn depends on the optics and sensor characteristics) are 0.001° for the streak endpoints and 0.0007° for the streak centers.

Because of the non-linearity of h, finding an optimum value for x_o^{lsq} is an iterative process. With each iteration, one obtains a new value for x_o and the loss function $J(x_o)$. One also obtains a 6×6 covariance matrix **P** that is determined by the observational errors for the state vector. The iterations proceed until the relative change of the loss function is smaller than some prescribed tolerance.

In the refinement of NORAD 27006, the initial approximation to x_o^{ref} was the J2000 inertial position and velocity state vector at the time of the first observation t_o. This was found by fitting the TLE from January 14, 2013 over a whole number of orbits in about a one day time span. The partial derivatives were all calculated numerically using the force model (described in the next section) with $\delta r_i = 5$ m and $\delta v_i = 0.01$ m s^{-1}. Three iterations were necessary before the solution converged at a value of x_o^{lsq}. This new state vector represents the refined orbit against which the measurements in the 5th and 6th observations were tested.

4.7. Force Model Propagating Orbit of Target to Time of Conjunction

The motion of a satellite in LEO is governed by a set of gravitational forces F_G and nongravitational forces F_{NG} according to Newton's Second Law:

$$F(t, r, v) = F_G + F_{NG} = m\ddot{r}.$$

Propagating the orbit of a satellite using a force-model consists of numerically time-evolving the state vector x by solving this equation with a set of initial conditions, usually in the form of an initial state vector x_o.[h] The accuracy of the orbit, of course, depends on how many terms are included in FG and FNG, and how well these terms are modeled. It also depends on the fidelity of the numerical integrator chosen.

4.7.1. Gravitational Forces

The model used to propagate SN27006 included the following gravitational terms:

$$F_G = F_{GEO} + F_{SM},$$

where

- F_{GEO} is is the geopotential force attributable to the gravitational attraction of the earth. The actual implementation was a 20×20 JGM-3 gravity model. In

[h] The actual implementation used here solves a slightly different differential equation that is first order in the state vector x. The time derivative of r is v and the time derivative of v is the sum of the accelerations. Using the accelerations removes the mass of the satellite from the equation.

Copyright © A. Deepak Publishing. All rights reserved.

this model, the gravitational moments of the earth are given in terms of the International Terrestrial Reference Frame (ITRF) coordinates, which are a realization of the International Terrestrial Reference System. Computationally efficient recursion relations are used to calculate the acceleration from the gravitational moments, and a set of time-varying Earth Orientation Parameters (EOP) are needed to transform this acceleration from ITRF to J2000 coordinates. The EOPs are calculated from the IAU 1976 Theory of Precession and IAU 1980 Theory of Nutation (Montenbruck and Gill, 2001).

- F_{SM} represents the Sun and Moon third body forces.

The STARE force model propagator can also incorporate the third body forces due to Venus, Mars, and Jupiter, and the forces due to the gravitational field perturbations from the earth solid body and ocean tides, but these two sets of forces were the only gravitational forces implemented for SN27006 because they are dominant for objects in LEO.

4.7.2. Non-Gravitational Forces

The only non-gravitational force included in the force model for SN27006 was atmospheric drag:

$$F_{NG} = F_{DRAG}.$$

This force typically overwhelms the other nongravitational forces for objects in LEO by orders of magnitude. The drag takes the form

$$\frac{dv}{dt} = -\frac{1}{2} C_D \frac{A}{M} \rho v_r^{\,2} e_v,$$

where the relative velocity vector v_r (in J2000 coordinates) is with respect to the velocity of the earth's atmosphere, which for no wind co-rotates with the earth. C_D is the coefficient of drag, ρ is the density of the atmosphere at the orbiting object's position, A is the effective cross-sectional drag area, and M is the mass. The unit vector e_v is in the direction of the relative velocity vector, and the minus sign is present because the drag is opposed to the relative velocity vector.

The atmospheric drag can be estimated using either an atmospheric model together with solar weather files and allowing $C_D A/M$ to vary or by specifying da/dt in m day^{-1}. The quantity da/dt, where a is the semi-major axis of the orbit and t is time, is always negative. It can be converted to a drag force by first relating it to dE/dt, where E is the total energy of the satellite, and then using this to obtain a dv/dt by applying the virial theorem. One can estimate da/dt by looking at historic TLEs. The historic TLEs for SN27006 gave da/dt=-0.13 m day^{-1} looking back one year and da/dt= -0.38 m day^{-1} looking back two years. The value used for the propagation was da/dt=- 0.25 m day^{-1}, the average of the two.

4.7.3. Time-Evolution of the Orbit to the Prediction Times

The numerical integrator used to time-evolve SN27006 from the initial state vector obtained from the fit to the times of the 5th and 6th observations was the DE numerical integrator (Montenbruck and Gill, 2001). The integration yielded two state vectors for each time: x_5^{start} , x_5^{end} and x_6^{start}, x_6^{end} . The vectors were transformed to equatorial coordinates, allowing for direct comparison to the RA and DEC values measured for the start and end track endpoints in the images from the 5th and 6th observations.

4.7.4. Other Force Models and Integrators

While specific choices were made for the force models and numerical integrator in the case of SN27006, the STARE force model propagator is not limited to these alone. It can use a variety of other numerical integrators. In addition, it can use the EGM-96 gravity model (NGA/NASA, 2013) and can use one of the Jacchia-Bowman 2008 (Bowman et al., 2008), NRL MISISE-00 (Picone et al., 2002), GOST 2004 (Volkov and Suevalov, 2005), Jacchia-Roberts 1971 (Jacchia, 1971; Roberts, 1971), and Harris-Priester (Harris and Priester, 1962) atmospheric models. Other gravitational and non-gravitational forces, such as solar radiation pressure, can easily be inserted as well. The fitting methodology and propagator have been extensively

Copyright © A. Deepak Publishing. All rights reserved.

tested on ground-based images (Nikolaev et al., 2011).

5. Results

The main result of the analysis, in the form of a comparison between a) the locations of the streak endpoints measured in images from the 5th and 6th observations and b) the locations of the streak endpoints predicted at the times of the 5th and 6th observations from the orbital refinement and propagation, is shown in the fifth column of Table 3. The differences in the RA and DEC angles, i.e. the errors, have been converted to a distance in meters by using the range of the STARE telescope to SN27006 at the time of the observations (in column 3). The largest difference is well below the 100 m accuracy sought by STARE.

In the rightmost column is a similar comparison, but this time it is between a) the locations of the streak endpoints measured in images from the 5th and 6th observations and c) the locations of the streak endpoints predicted at the times of the 5th and 6th observations by fitting an orbit to the NORAD TLE released nearest to those times and propagating it ahead using the same methodology as described in the previous sections. The errors, while not quite at the 1 km level, are more than ten times as large as the ones from the STARE prediction.

Although the latter errors provide an indication of how good the STARE predictions are, they do not provide the error along the line of sight. However, the NTW covariance matrices at the observation times make calculation of the instantaneous along-track and cross-track rms errors straightforward.[i] Recall that a covariance matrix is always obtained from the batch force iIn NTW, T is the unit vector along the ECI velocity vector, W is the out-of-plane unit vector in the direction of the angular momentum L, and the unit vector N is defined so as to make NTW an orthogonal right-handed triad of unit vectors. model least squares fitting, and is completely determined by the observations and their measurement errors. This covariance matrix can be propagated to different times using the dx/dxo partial derivatives matrix along with the force model.

For the *evolution* of the errors, the equinoctial covariance matrix elements $\langle da\ da \rangle$, $\langle da\ d\lambda \rangle$, and $\langle d\lambda\ d\lambda \rangle$ are used. Here, a is the semi-major axis length, $\lambda = M + \varpi + \Omega$ is the mean longitude, M is the mean anomaly, ϖ is the argument of perigee, and Ω is the right ascension of the ascending node. In particular, the along-track errors at exactly the observation times are approximately the square root of $((\langle d\lambda\ d\lambda) a)$, assuming a nearly circular orbit. The along-track and cross-track (including along the line of sight) errors are shown in columns 6 and 7 of Table 3.

It can be seen from Table 3 that the fit errors for the 5th and 6th observations are comparable to what is expected from the NTW covariance matrix at the respective observation times. Furthermore, both the cross-track and along-track errors are well within the 100 m accuracy as well.

Figure 5 illustrates the information contained in Table 3 in visual form. The various types of measurements and predictions for the 5th and 6th observations are represented with overlaid circles centered on the respective coordinate centers. The colors used for each circle correspond with those in Table 3. One can see that the endpoints measured in each image by the STARE algorithm (magenta) match up almost perfectly with the ones predicted by using the first four observations (green). The circles centered on the TLE predictions (teal) are also given. These lie much further away from the true endpoints.

Figure 6 shows a zoomed-in version of the endpoints in the previous figure. Now the dashed circles are drawn with the sizes indicating the respective rms values. This figure illustrates the improvement in the predictions derived from the STARE approach over those obtained by propagating the available TLEs.

There is one additional way to look at the data that provides further indication for the potential of STARE. As mentioned, STARE will typically make 5-10 observations of a target for refinement. If all six observations of SN27006 are used to fit its orbit, instead of using the first four to predict the last two, the fit accuracy is approximately equal to the measurement ac-

[i] In NTW, T is the unit vector along the ECI velocity vector, W is the out-of-plane unit vector in the direction of the angular momentum L, and the unit vector N is defined so as to make NTW an orthogonal right-handed triad of unit vectors.

Copyright © A. Deepak Publishing. All rights reserved.

Table 3. Endpoint errors for the 5th and 6th STARE observations. One can see that the coordinates predicted with the STARE measurements are all within 100 m of the measured coordinates while the TLE predictions are much further off.

Observation	Delay [hours]	Distance from STARE telescope to Satellite* [km]	Endpoint	Error in STARE Prediction vs. Measured [m]	STARE Prediction RMS Uncertainty in Cross-Track Direction [m]	STARE Prediction RMS Uncertainty in Along-Track Direction [m]	Error in TLE Prediction vs. Measured [m]
5th	12.75	1526.737-1529.293	START	24.9	27	32	520.75
			END	54.6	27	32	614.64
6th	35.5	1277.265-1279.703	START	30.0	29	45	575.74
			END	29.3	29	45	526.34

curacy (0.001° for the streak endpoints and 0.0007° for the streak centers). The measurement accuracy for the streak endpoints, which is about 0.2-1.0 pixels depending on the streak brightness, is more than sufficient to meet the 100 m requirement. However, if increased accuracy in the orbital refinement is desired, it could be increased with a larger/better set of optics, or a more sensitive sensor with 100% fill factor.

6. Discussion

The predictions made with the STARE data are far more accurate than those made with the TLE. More importantly, they are well within the 100 m accuracy required for the STARE mission. One might note that SN27006 is a very bright object and that it is quite high above the Earth. Indeed, two important factors that will determine the limitations of STARE's reach will be atmospheric drag and object brightness. Each will be discussed in turn.

6.1. Atmospheric Drag

Uncertainties in the atmospheric drag will be what practically limits how far into the future accurate position predictions may be made. It is straightforward to show that the along-track deviation due to drag increases quadratically in time for constant da/dt according to the equation

$$\Delta s = \frac{3\pi}{2}\left(\frac{da}{d\text{day}}\right)\left(\frac{\text{orbits}}{\text{day}}\right)(\text{days}^2).$$

Note that the derivation assumes a circular orbit, but the quadratic relationship holds for elliptical orbits as well. Here Δs has the same units as the semi-major axis length a. If the orbiting object's position is ahead of what it would have been had there been no drag, then Δs is positive.

Perhaps the most accurate atmospheric models based solely upon solar radiation and particle flux observations is the Jacchia-Bowman 2008 model (Bow-

Copyright © A. Deepak Publishing. All rights reserved.

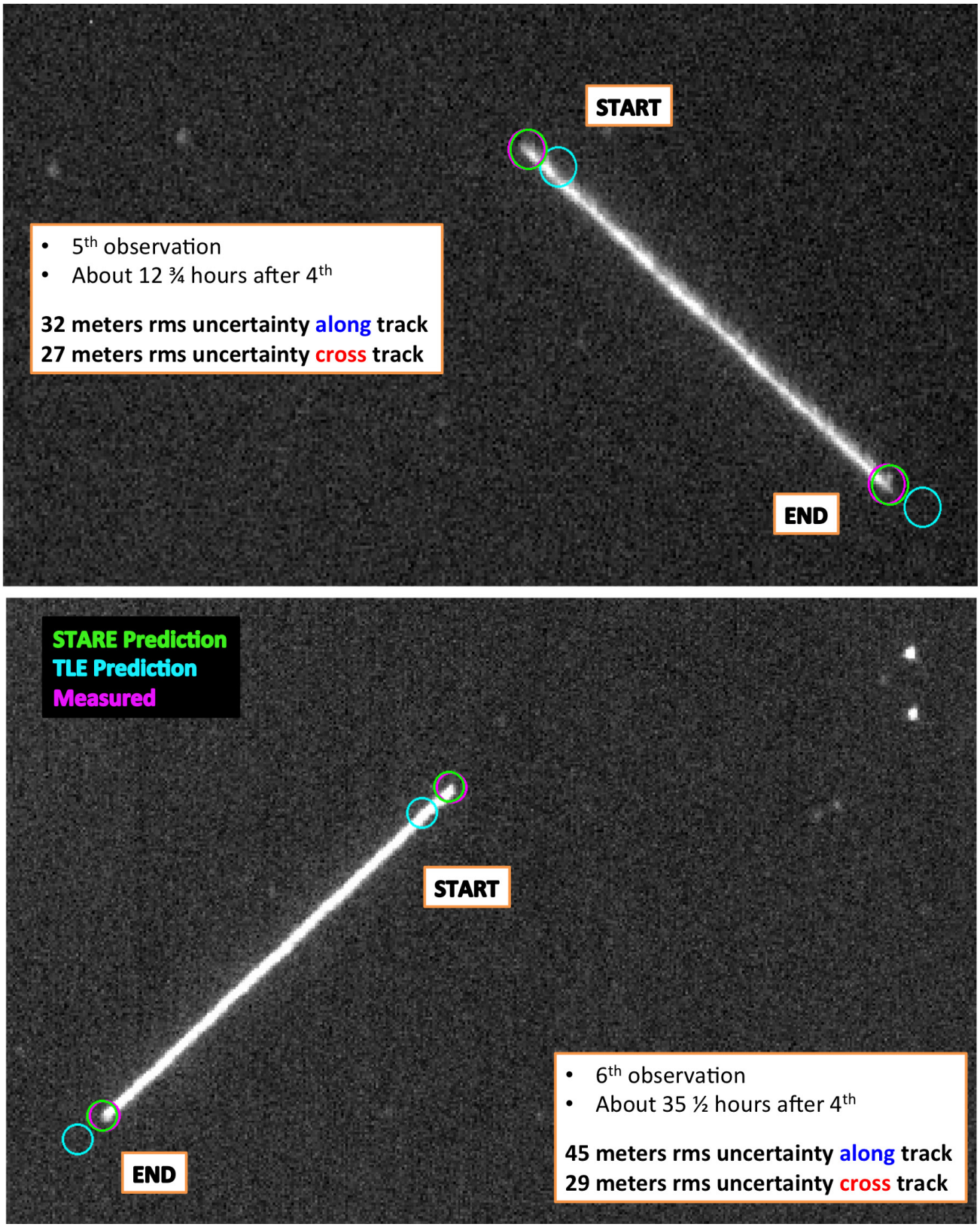

Figure 5. A set of processed images depicting the coordinates involved in the ground campaign with SN27006. The green and magenta circles, almost on top of each other, show the locations of the coordinates predicted by the STARE observations and those measured in the processed images by the STARE algorithm, respectively. The teal circles that lie further away from the true endpoints are those predicted by the TLEs.

Copyright © A. Deepak Publishing. All rights reserved.

man et al., 2008). It computes the thermosphere and exosphere atmospheric heating based not only upon the solar UV and Xray flux as measured by satellites, but also upon the particle flux based upon measurements of the magnetic field changes *Dst* (the disturbance storm time index) in nano-teslas made by four stations near the equator monitoring the ionospheric ring current and based upon measurements of the planetary magnetic indices, *Ap*, made by high latitude stations. These observations are combined into a temperature correction, *DstTC*, due to the solar particle flux. During quiet times, only the geoplanetary magnetic indices, *Ap*, are used to obtain *DstTC*. But during a magnetic storm, a differential equation is solved using the Dst values to obtain *DstTC*.

The Air Force's High Accuracy Satellite Drag Model (HASDM) has greater accuracy than the Jacchia-Bowman 2008 model because it is based upon observations of the orbital decay of a large number of satellites of known shapes, attitudes, and masses (Storz et al., 2005). Though not publicly available, it computes a density correction to the Jacchia-Roberts atmospheric model.

When the atmospheric drag is small, it suffices to use a model with fixed da/dt. Small is defined as s being less than 200 m over the combined observation and prediction time period. When atmospheric drag is not

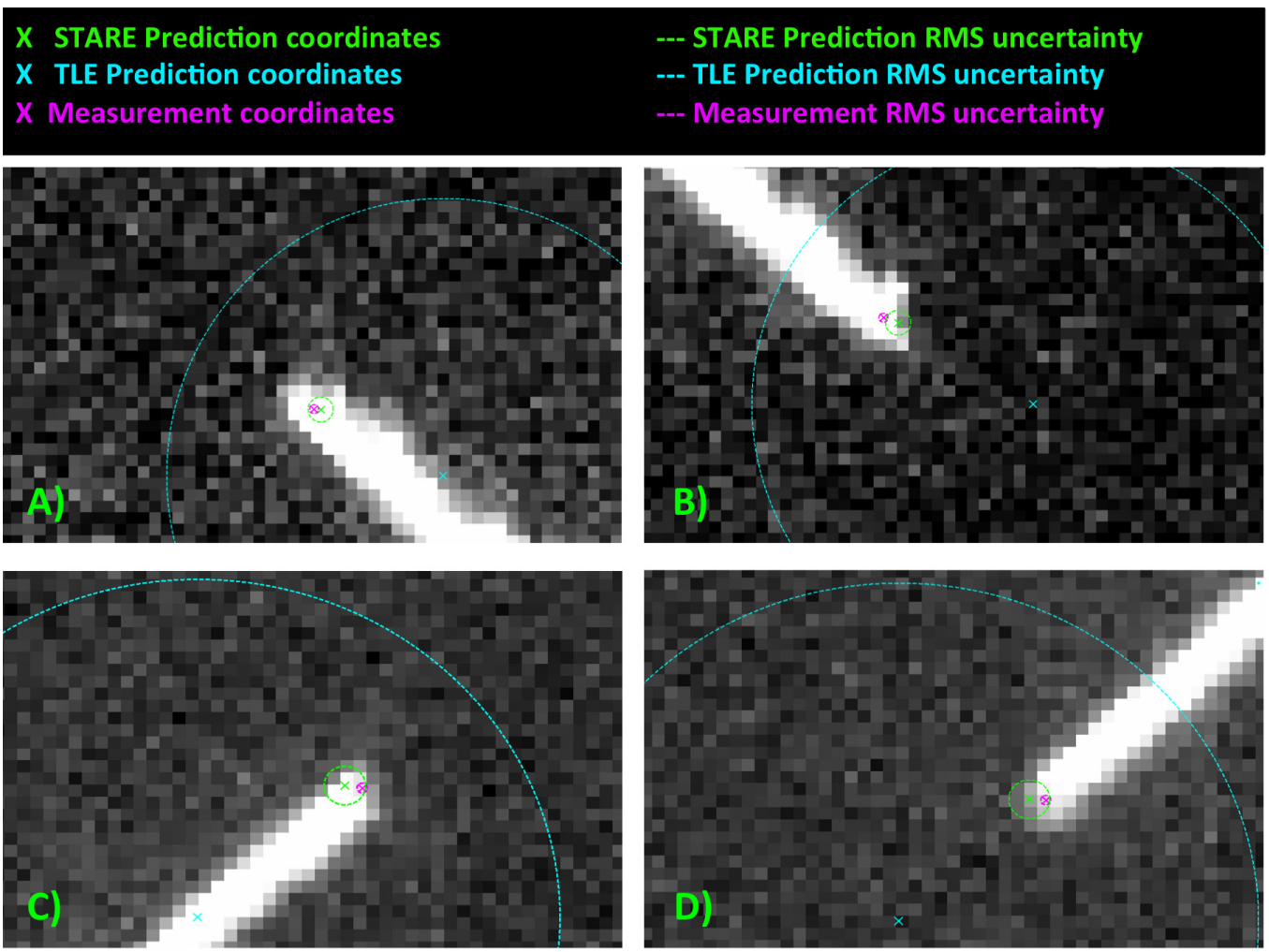

Figure 6. Zoom-in images of track endpoints for SN27006. The very small dashed magenta circle shows the uncertainty associated with the STARE endpoint detection algorithm, the slightly larger green circle shows the uncertainty in the prediction made with the first four STARE observations, and the largest teal circle shows the uncertainty inherent in the TLE predictions. The X's at the center of the circles show the coordinates for each of the latter measurements/predictions. A) and B) are the start and end of the track from the 5th observation, respectively. C) and D) are the start and end of the track from the 6th observation, respectively.

Copyright © A. Deepak Publishing. All rights reserved.

Table 4. Extrapolation of STARE performance for lower SNR objects. The lower SNR in the second row and below occurs because of a smaller surface area. However, this smaller surface area can be offset by a smaller target distance or relative velocity, which keeps the SNR constant.

Surface Area rel. to SN27006	Magnitude/pixel	Target/distance [km]	Relative velocity [km/s]	ADU transverse	Streak Length [pixels]	SNR transverse
1.000	9.13	1204	7.156	447.2	219.7	41.4
1.20210-1	11.43	1204	7.156	54.0	219.7	5.0
9.98610-3	11.43	100	7.156	54.0	2645.2	5.0
1.39510-3	11.43	100	1.000	54.0	396.6.	5.0
5.58010-4	12.43	100	1.000	21.6	396.6	2.0

small, the most accurate atmospheric model available should be used and force model batch least squares fits on a grid of $C_D A/M$ values should be applied. From the historic TLE's, a bound for the most negative da/dt can be determined. Then, from the atmospheric model, the orbit, and this most negative da/dt bound, a bound for $C_D A/M$ can in turn be determined. For objects at lower altitude than SL-16, the errors in prediction will be larger and will require measurements made closer to the time of conjuction.

6.2 Object Brightness and Sensitivity

The SL-16 rocket booster is a rather large cylindrical target, at 3.9 m × 32.9 m. However, most of the debris targets that STARE will have to observe are considerably smaller. As a first order estimate, one can scale the SN27006 observations to the current limit of the STARE V2 optics in order to assess the smallest piece it is likely able to observe.[j]

Using the first image of the sequence (14JAN2013, 13:56 UTC), an unfiltered magnitude zero-point for the V2 optics of 15.76±0.13 is derived. This is done using the many field stars in the image, in combination with their known brightnesses. The zero-point just means that a single count in a single pixel per secnd corresponds to a 15.76 magnitude object. However, given the actual Point-Spread Function (PSF) of the optic, the signal gets spread out among roughly a 6 × 6 pixel area, and the faintest identified stars are about 11th magnitude. In other words, about 50 counts per PSF are needed for a positive identification (formally a 5 sigma detection).

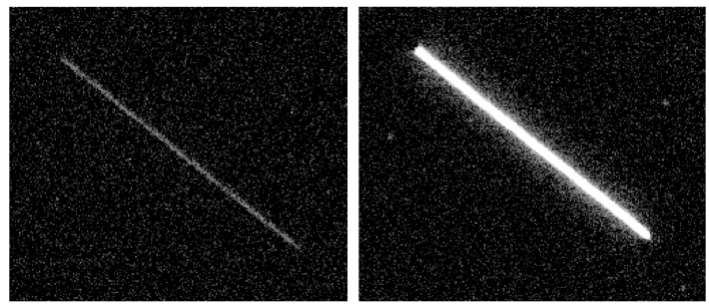

Figure 7. The actual 27006 streak (14Jan2013 13:56) is shown on the right. It has an SNR of 40 per unit length. Since the length of the streak is 219 pixels, the total signal in the streak exceeds 9000 × the local noise value. On the left-hand side, the streak has been scaled down to a SNR=2 level per unit length. This represents about the faintest streak for which the STARE algorithm can accurately determine end-points

Streaks, on the other hand, can be identified at fainter signal levels by virtue of their shape; it is easier to detect interconnected pixels. In Figure 7, the actual track with SNR of more than 40 (per unit length) has been scaled down to a SNR=2 track. The endpoint detection algorithm can correctly identify the endpoints of these kinds of streaks to better than 1 pixel.

The brightness of the streak, aside from the solar illumination, is set by the size of the target, the distance to the target, and the angular velocity relative to the detector. Since the STARE telescope is tracking stars, the object will streak through the field of view, and the dwell-time per pixel is what matters. Therefore, for a realistic comparison (see Table 4), one must also account for the fact that being closer decreases the effective integration time per pixel linearly, even though the brightness increases quadratically. The main limitation

[j] There are three STARE prototype satellites, each of which has a different payload configuration: V1, V2, and V3. V2 and V3 use the same sensor, but V3 has a better set of optics. A V2 payload took all measurements described here.

Copyright © A. Deepak Publishing. All rights reserved.

here is that the length of the streak will quickly exceed the available field-of-view, making it impossible to determine end-points. The relevant scalings are listed in Table 4.

Therefore, based on the SN27006 observations, the faintest streak has a surface area that is about 5.6×10^{-4} times as small. In linear terms, this translates into a cylinder of 0.092 m diameter by 0.777 m long.

If one assumes the cylinder is fully illuminated by the Sun, and scatters like a Lambertian surface, an equivalent square area of 0.19 m × 0.19 m is derived as the smallest object the STARE V2 telescope can possibly detect. It should be noted that the STARE V2 requirements are being able to detect a 1 m × 1 m object at 100 km and 1 km s^{-1} transverse velocity, so it easily meets this requirement.

7. Conclusion

The results obtained with the STARE telescope from the ground are highly encouraging. The two predictions made over a 36-hour period for SN27006 using a previous set of four observations taken over a 24-hour period are well within the 100 m accuracy goal of STARE. Additional observations made before the last two would have helped reduce the uncertainty further, as evidenced by using all six observations to fit the orbit. Extrapolations based on this data set show that the STARE telescope will readily observe fainter targets.

Acknowledgments

Lawrence Livermore National Laboratory is operated by Lawrence Livermore National Security, LLC. for the U.S. Department of Energy, National Security Administration under Contract DE-AC52-07NA27344.

References

Bowman, B. R., et al., (2008): A New Empirical Thermospheric Density Model JB2008 using New Solar and Geomagnetic Indices, in Proc. *Astrodynamics Specialist Conference*, Honolulu, HI.

Haines, L. and Phu, P. (2011): Space Fence PDR Concept Development Phase. in Proc. *Advanced Maui Optical and Space Surveillance Technologies Conference*, Maui, HI.

Harris, I. and Priester, W. (1962): Time-Dependent Structure of the Upper Atmosphere. *Journal of the Atmospheric Sciences,* 19(4), pp. 286–301.

Jacchia, L. G. (1971): Revised Static Models of the Thermosphere and Exosphere with Empirical Temperature Profiles. *SAO Special Report*, 332.

Montenbruck, O. and Gill, E. (2001): *Satellite Orbits: Models, Methods, and Applications*, New York: Springer.

NGA/NASA (2013): NGA/NASA EGM96, n=m=360 Earth Gravitational Model. Retrieved on 6/11/13: http://earthinfo.nga.mil/GandG/wgs84/gravitymod/egm96/egm96.html.

Nikolaev, S., et al. (2011): Analysis of Galaxy 15 Satellite Images from a Small-Aperture Telescope, in Proc *Advanced Maui Optical and Space Surveillance Technologies Conferenc*e, Maui, HI.

Picone, J. M., et al. (2002): NRL-MSISE-00 Empirical Model of the Atmosphere: Statistical Comparisons and Scientific Issues, *Journal of Geophysical Research*, 107(A12), pp. SIA 15-1–SIA 15-16.

Roberts, Jr., C. E. (1971): An Analytic Model for Upper Atmosphere Densities based upon Jacchia's 1970 Models, *Celestial Mechanics*, 4(3,4), pp. 368–377.

Simms, L. M., et al. (2012): Space-Based Telescopes for Actionable Refinement of Ephemeris Pathfinder Mission, *Optical Engineering,* 51(1), pp. 011004-1–011004-13.

Storz, M. F., et al. (2005): High Accuracy Satellite Drag Model (HASDM), *Advances in Space Research,* 36(12), pp. 2497–2505.

Vallado, D. A. (2005). An Analysis of State Vector Propagation Using Different Flight Dynamics Programs. in Proc. *AAS/AIAA Space Flight Mechanics Conference,* Copper Mountain, CO.

Vallado, D. A. and Finkleman, D. (2008): A Critical Assessment of Satellite Drag and Atmospheric Density Modeling, in Proc. AIAA/AAS *Astrodynamics Specialist Conference*, Honolulu, HI.

Vetter, J. R. (2007): Fifty Years of Orbit Determination: Development of Modern Astrodynamics Methods,

Copyright © A. Deepak Publishing. All rights reserved.

Johns Hopkins APL Techincal Digest, 27(3), pp. 239–252.

Volkov, I. I. and Suevalov, V. V. (2005). Estimation of Long-Term Density Variations in the Upper Atmosphere of the Earth at Minimums of Solar Activity from Evolution of the Orbital Parameters of the Earth's Artificial Satellites, *Solar System Research,* 39(2), pp. 157–162.

Copyright © A. Deepak Publishing. All rights reserved.